Inorganic Chemistry

Article

pubs.acs.org/IC

Microwave-Assisted Synthesis of Defects Metal-Imidazolate-Amide-Imidate Frameworks and Improved CO_2 Capture

Karsten Behrens,[†] Suvendu Sekhar Mondal,[*,†] Robert Nöske,[†] Igor A. Baburin,[‡] Stefano Leoni,[§] Christina Günter,[∥] Jens Weber,[⊥] and Hans-Jürgen Holdt[*,†]

[†]Institut für Chemie, Anorganische Chemie, Universität Potsdam, Karl-Liebknecht-Straße 24-25, 14476 Potsdam, Germany

[‡]Institut für Physikalische Chemie und Elektrochemie, Technische Universität Dresden, Dresden 01062, Germany

[§]Cardiff University, School of Chemistry, Cardiff CF10 3AT, United Kingdom

[∥]Institut für Erd- und Umweltwissenschaften, Universität Potsdam, 14476 Potsdam, Germany

[⊥]Department of Chemistry, Hochschule Zittau/Görlitz, University of Applied Science, 02763 Zittau, Germany

Supporting Information

ABSTRACT: In this work, we report three isostructural 3D frameworks, named **IFP-11** (R = Cl), **IFP-12** (R = Br), and **IFP-13** (R = Et) (IFP = Imidazolate Framework Potsdam) based on a cobalt(II) center and the chelating linker 2-substituted imidazolate-4-amide-5-imidate. These chelating ligands were generated *in situ* by partial hydrolysis of 2-substituted 4,5-dicyanoimidazoles under microwave (MW)-assisted conditions in DMF. Structure determination of these IFPs was investigated by IR spectroscopy and a combination of powder X-ray diffraction (PXRD) with structure modeling. The structural models were initially built up from the single-crystal X-ray structure determination of **IFP-5** (a cobalt center and 2-methylimidazolate-4-amide-5-imidate linker based framework) and were optimized by using density functional theory calculations. Substitution on position 2 of the linker (R = Cl, Br, and Et) in the isostructural **IFP-11**, **-12**, and **-13** allowed variation of the potential pore window in 1D hexagonal channels (3.8 to 1.7 Å). The potential of the materials to undergo specific interactions with CO_2 was measured by the isosteric heat of adsorption. Further, we resynthesized zinc based IFPs, namely **IFP-1** (R = Me), **IFP-2** (R = Cl), **IFP-3** (R = Br), and **IFP-4** (R = Et), and cobalt based **IFP-5** under MW-assisted conditions with higher yield. The transition from a nucleation phase to the pure crystalline material of **IFP-1** in MW-assisted synthesis depends on reaction time. **IFP-1**, **-3**, and **-5**, which are synthesized by MW-assisted conditions, showed an enhancement of N_2 and CO_2, compared to the analogous conventional electrical (CE) heating method based materials due to crystal defects.

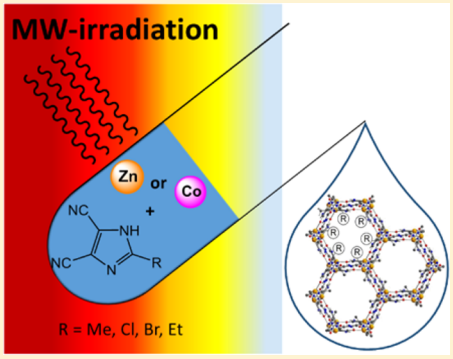

INTRODUCTION

The emission of CO_2 is one of the crucial issues for the energetic use of fossil fuels with the correlation seen for increased atmospheric CO_2 content and global warming.[1,2] Research on selective carbon capture and storage is currently receiving high attention to reduce the emission of greenhouse gases such as CO_2 in the environment. Carbon (dioxide) capture and reuse or storage are debated technologies, thereby also taking into account CO_2 as a valuable precursor for (possible) industrial chemical syntheses or physical processes (e.g., urea synthesis, use as a coolant, or in enhanced oil recovery).[1] In the past two decades, a new class of crystalline porous materials, metal−organic frameworks (MOFs), has emerged, and the associated research has been developed into one of the most prolific areas in chemistry and materials science.[3−7] MOFs are comprised of metal-containing nodes linked by organic ligand bridges and assembled principally through strong coordination bonds. MOFs have geometrically and crystallographically well-defined framework structures, and in most cases, these structures are robust enough to allow the removal of the included guest species resulting in permanent porosity. They have been traditionally prepared by conventional electrical (CE) heating methods (solvo- or hydrothermal) with temperatures varying from room temperature up to 200 °C and the duration of reaction time from hours to days. Also, alternate techniques established in the past decade, such mechanochemistry,[8] electrochemical methods,[9] aerosol methods,[10] ultrasonic (US) methods,[11] and microwave (MW)-assisted synthesis.[12]

To enhance the CO_2 capture with MOFs, various strategies have been developed such as pore-surface functionalization with amines,[13,14] making the network flexible,[15] using organic ligands with flexible joints[16] and side chains,[17] creating accessible metal sites[18] and rotatable pillared-layer based frameworks,[19] and exposing Lewis base sites[20] as well as recently defective MOFs[21] with improved adsorption capacities. The defects in MOFs have been defined as the sites that locally

Received: August 24, 2015
Published: October 8, 2015

DOI: 10.1021/acs.inorgchem.5b01952
Inorg. Chem. 2015, 54, 10073−10080

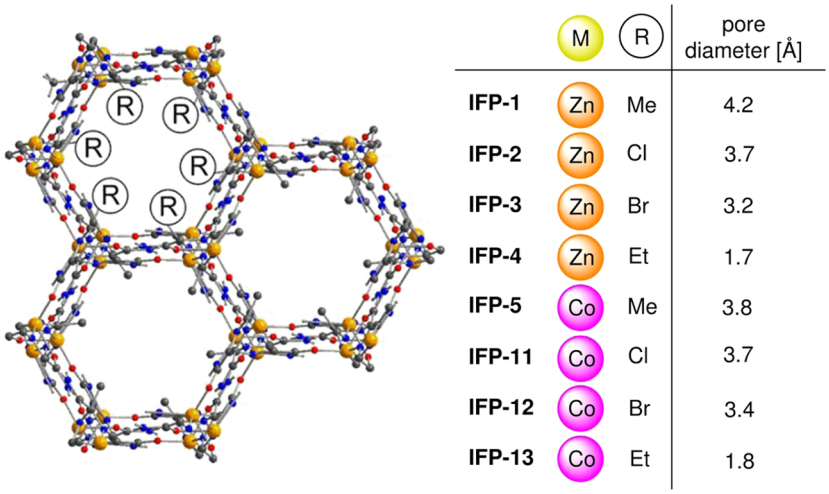

Figure 1. Isostructural series of IFPs with hexagonal channels. The substituents of the linker are presented as R (the potential pore channel diameter was estimated by considering van der Waals radii).

break the regular periodic arrangement of atoms or ions of the static crystalline parent framework because of missing or dislocated atoms or ions.[21a] Introduction of defect sites into ordered structures is also a useful strategy to realize unusual heterogeneous structures and properties. For example, the formation of missing linker defective $[Zr_6O_4(OH)_4(BTC)_6]$ (UiO-66) systems as a consequence of the use of acidic modulating agents (HCl, MeCOOH, HCOOH) during its synthesis is also the subject of intensive debate about the molecular nature of the defects and its impact in its properties.[21d] The solvent-assisted linker exchange, postsynthetic acid treatment by Brönsted acid sites, utilization of modulator molecules, and reaction quenching concepts have been demonstrated as an important strategy to create the defect structure and/or dynamic defects of the parent frameworks.[21e] Furthermore, the systematic studies of gas adsorption properties (N_2 and CO_2) in MOFs containing a large number of diverse organic links have been reported already.[22] Similar efforts on isostructural MOFs containing different metal coordination sites are limited to only a handful of systems, such as **CPO-27M** [M = Zn, Co, Ni, and Mg][23] with open metal sites inside the framework and **ZIF-68**, **-69**, **-81** [M = Zn and Co].[24] Hence, an extensive study on a large number of systems is needed to completely understand the effects of metal replacement on gas sorption properties in MOFs.

We have previously reported the synthesis of the metal-amide-imidate-imidazolate neutral 3D framework with 1D hexagonal channels, named IFP (**IFP-1** to **-5** and **-7** to **-10**; IFP = Imidazolate Framework Potsdam).[25] Such types of chelating ligands, amide-imidate-imidazolate, were generated *in situ* by partial hydrolysis of 2-substituted 4,5-dicyanoimidazole under CE heating conditions in *N*,*N*′-dimethylformamide (DMF) and in the presence of metal nitrate hydrate salts. Herein, we report the synthesis of three cobalt based IFP structures named **IFP-11**, **-12**, and **-13** that are synthesized exclusively under MW-assisted conditions. These IFPs (**IFP-11**, **-12**, and **-13**) are isostructural to the three reported zinc based **IFP-2**, **-3**, and **-4**, respectively, with the same *etb* topology and similar pore apertures.[25] In addition, previously reported zinc based **IFP-1** to **-4** and cobalt based **IFP-5** are resynthesized under MW-assisted conditions. This type of metal replacement in the isostructural frameworks and different synthetic reaction conditions motivates us to understand the role of metals on CO_2 binding at the MOFs pore surface and crystal defects of the materials.

EXPERIMENTAL SECTION

Materials and Synthesis. The linker precursors 4,5-dicyano-2-methylimidazole (**1a**),[26a] 2-chloro-4,5-dicyanoimidazole (**1b**),[26b] 2-bromo-4,5-dicyanoimidazole (**1c**),[26c] and 4,5-dicyano-2-ethylimidazole (**1d**)[26a] were synthesized according to the published procedures. All reagents and solvents were used without further purification. MW-assisted synthesis was performed on the microwave system CEM*Discover*. For general synthesis, 50 mg of the linker precursor **1a**−**1d** and an equimolar amount of metal salt hydrates were dissolved in DMF and placed in a 10 mL glass vial with a magnetic stirrer. Under MW-assisted conditions, the Zn(II)- and Co(II)-based imidazolate frameworks are formed, filtrated, and washed with DMF and water (see Supporting Information (SI) for details).

IFP-11. A total of 50 mg (0.33 mmol) of **1b** and 72 mg (0.33 mmol) $Co(OAc)_2{\cdot}4H_2O$ were dissolved in 3 mL of DMF. Under MW conditions at 150 °C and 30 min of reaction time, pale purple powder was obtained. Yield: 54 mg (75%) based on $Co(OAc)_2{\cdot}4H_2O$; elemental analysis for $C_5H_3ClN_4O_2Co{\cdot}0.5H_2O$: C 23.60, H 1.58, N 22.02, Co 23.16. Found: C 23.92, H 1.48, N 21.73, Co 23.85. IR (KBr pellet): 3337, 3276, 3118, 2925, 2854, 2794, 1659, 1549, 1461, 1336, 1256, 1110, 1051 cm^{-1}.

IFP-12. A total of 50 mg (0.25 mmol) of **1c** and 56 mg (0.25 mmol) of $Co(OAc)_2{\cdot}4H_2O$ were dissolved in 3 mL of DMF. Under MW conditions at 140 °C and 60 min of reaction time, purple powder was obtained. Yield: 53 mg (72%) based on $Co(OAc)_2{\cdot}4H_2O$; elemental analysis for $C_5H_3BrN_4O_2Co{\cdot}0.5H_2O$: C 20.02, H 1.68, N 18.68, Co 19.65. Found: C 20.60, H 1.89, N 17.94, Co 20.09. IR (KBr pellet): 3335, 3290, 3129, 2788, 1659, 1550, 1461, 1315, 1253, 1110, 1027 cm^{-1}.

IFP-13. A total of 50 mg (0.34 mmol) of **1d** and 75 mg (0.34 mmol) of $Co(OAc)_2{\cdot}4H_2O$ were dissolved in 3 mL of DMF. Under MW conditions at 130 °C and 30 min of reaction time, fine dark purple powder was obtained. Yield: 61 mg (76%) based on $Co(OAc)_2{\cdot}4H_2O$; elemental analysis for $C_7H_8N_4O_2Co{\cdot}1H_2O$: C 32.70, H 3.92, N 21.79, Co 22.92. Found: C 32.42, H 3.37, N 21.70, Co 23.16. IR (KBr pellet): 3323, 3108, 2974, 2942, 2775, 1650, 1549, 1460, 1284, 1257, 1228, 1112 cm^{-1}.

RESULT AND DISCUSSION

Synthesis and Structure Determination. To reduce the reaction time and to obtain materials in good quality and higher yields, MW-assisted synthesis is one of the options for synthesizing MOFs materials.[12] However, we have reported

DOI: 10.1021/acs.inorgchem.5b01952
Inorg. Chem. 2015, 54, 10073−10080

Scheme 1. MW-Assisted Synthesis of IFP-1 to -5[25] and IFP-11 to -13

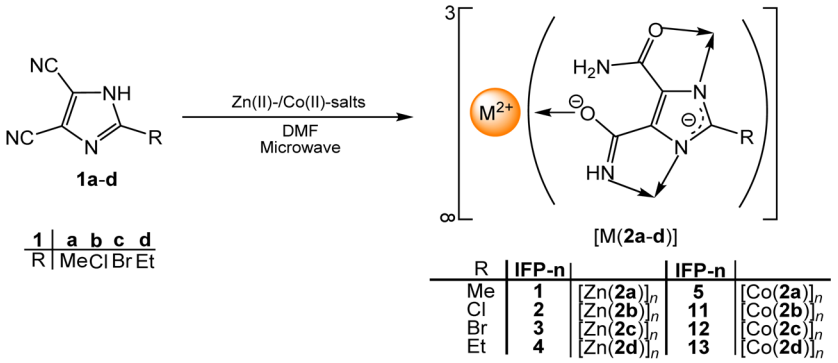

1	a	b	c	d
R	Me	Cl	Br	Et

R	IFP-n		IFP-n	
Me	1	$[Zn(\mathbf{2a})]_n$	5	$[Co(\mathbf{2a})]_n$
Cl	2	$[Zn(\mathbf{2b})]_n$	11	$[Co(\mathbf{2b})]_n$
Br	3	$[Zn(\mathbf{2c})]_n$	12	$[Co(\mathbf{2c})]_n$
Et	4	$[Zn(\mathbf{2d})]_n$	13	$[Co(\mathbf{2d})]_n$

zinc based isostructural IFPs (R = Me, **IFP-1**; R = Cl, **IFP-2**; R = Br, **IFP-3**; R = Et, **IFP-4**) that were formed under CE conditions in DMF (Figure 1).[25a,b] To achieve the isostructural cobalt based IFPs, the solvothermal CE reactions with the linker precursors **1b**−**1d** and cobalt hydrate salts failed to produce new isostructural IFP frameworks. Interestingly, cobalt based IFPs could only be synthesized under MW-assisted conditions in DMF (Scheme 1 and Figure 1). These materials are named **IFP-11** (R = Cl), **IFP-12** (R = Br), and **IFP-13** (R = Et). We anticipated that the rapid heating and the creation of hot spots or transient temperature and pressure gradients are important factors for the exclusive synthesis of Co(II)-IFPs under MW irradiation.[27]

Even after several attempts at MW-assisted syntheses, no suitable crystal for single X-ray diffraction was obtained for **IFP-11** to **-13** (see below for microscopy results). Hence, the structural model of these IFPs was constructed by using the single-crystal X-ray structure determination for **IFP-5**[25c] and was further optimized by using a density functional theory *ab initio* method (see SI for details). Moreover, the powder X-ray diffraction (PXRD) patterns of the optimized **IFP-11** to **-13** structures showed a good agreement with the experimental data (Figure 2 and Figures S13−15 in the SI). The theoretically

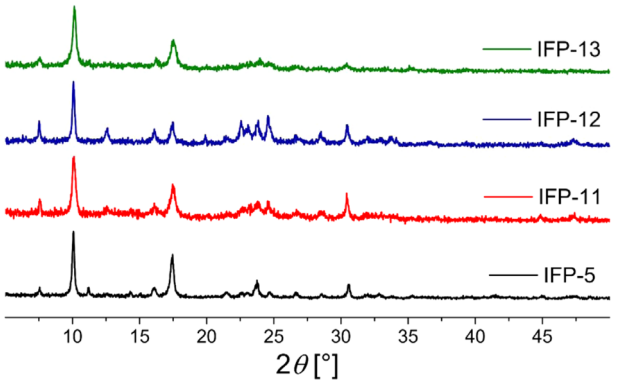

Figure 2. Comparison of the powder X-ray patterns of the Co(II) frameworks (from bottom to top): **IFP-5** (black), **IFP-11** (red), **IFP-12** (blue), and **FP-13** (green).

estimated structure of IFPs possesses 1D hexagonal channels (Figure 1). The substituent R groups of three linkers protrude into the open channels and form a regularly recurrent pore window. The potential pore window was calculated by considering the van der Waals radii. The theoretical void spaces in **IFP-11**, **-12**, and **-13** represent 41.7, 40.1, and 29.4%, respectively. These results are comparable to the isostructural Zn(II)-IFPs (**IFP-1** to **-4**).[25b] For the void space calculation, the PLATON toolkit was used.[28] The zinc based isostructural IFPs (**IFP-1** to **-4**) reported by us earlier were formed under CE conditions in DMF.[25b] We were furthermore interested in an understanding of the effects of these different synthesis methods, comparable to the work reported on **CPO-27M** (Zn, Ni, and Co).[23] We have resynthesized zinc based IFPs (**IFP-1** to **-4**) and cobalt based **IFP-5** under MW-assisted conditions in higher yields in the short reaction time, comparing with CE conditions. The yields of IFP materials, synthesized in MW-assisted conditions, are in the range of 72 to 82% (see Table S1, in the SI). The PXRD patterns of the resultant materials showed a positive matching and crystalline integrity, comparing with the material synthesized under solvothermal conditions (Figures S8−S16 in the SI).

Impact of Reaction Time. To check the influence of the reaction time on the crystallinity and the material formation mechanism, the MW-assisted synthesis of **IFP-1** is chosen as a model system. By varying the reaction time duration from 10 to 60 min at 120 °C under MW-assisted conditions in DMF, linker **1a** and $Zn(NO_3)_2{\cdot}4H_2O$ formed a fine crystalline powder material. The yield of **IFP-1** is reaction time-dependent. The maximum in yield is observed in the range of 80 to 85% after 25 min (Figure S1 in the SI). The PXRD pattern of resulting materials at different reaction times is presented in Figure 3. The transition from a nucleation phase into the pure crystalline material is observed after 40 min reaction time. The SEM images reveal that the small spherical particles that are obtained

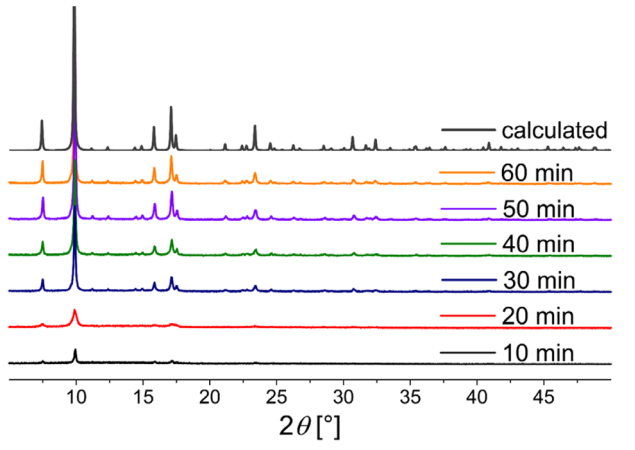

Figure 3. PXRD patterns of **IFP-1** synthesized by different reaction times under MW conditions.

DOI: 10.1021/acs.inorgchem.5b01952
Inorg. Chem. 2015, 54, 10073−10080

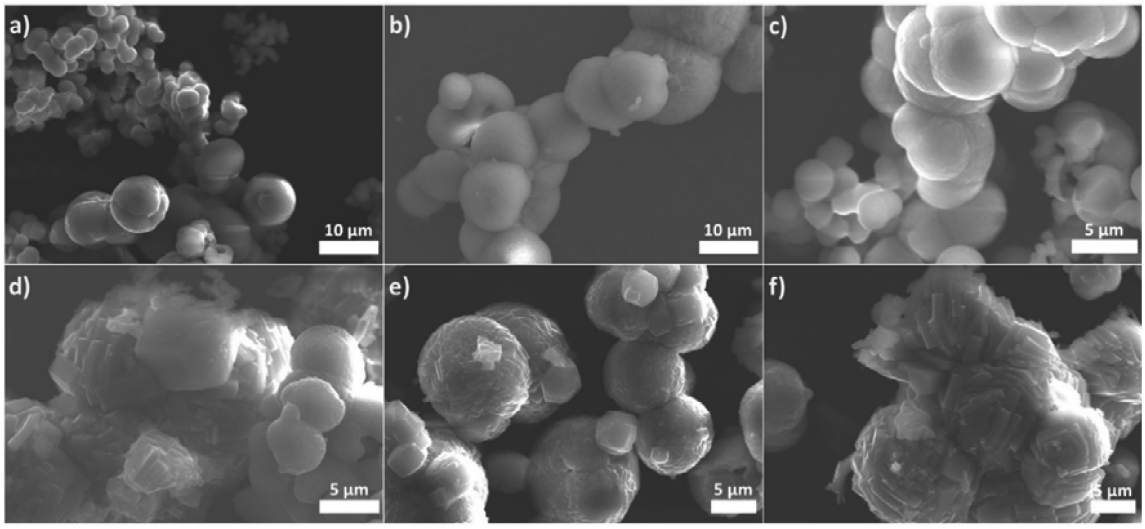

Figure 4. SEM images of **IFP-1**, synthesized by different reaction times under MW-conditions [(a) 10 min, (b) 20 min, (c) 30 min, (d) 40 min, (e) 50 min, (f) 60 min], showing the transition from a nucleation phase into the pure crystalline material.

Table 1. Particle Sizes of IFP-1 Depending on Statistical Distribution *Q*

	particle size d [μm]			
t [min]	D10[a]	D50[a]	D90[a]	D100[a]
10	5.43 ± 0.17	9.12 ± 0.21	15.12 ± 0.44	25.16 ± 0.65
20	4.64 ± 0.37	9.72 ± 0.37	16.78 ± 0.53	26.29 ± 0.29
30	6.15 ± 0.24	10.64 ± 0.31	16.86 ± 0.61	26.21 ± 1.68
40	7.32 ± 0.26	12.15 ± 0.18	19.02 ± 0.41	29.94 ± 0.63
50	7.96 ± 0.32	12.84 ± 0.19	19.96 ± 0.29	30.78 ± 0.79
60	7.36 ± 0.98	13.47 ± 0.57	23.26 ± 0.10	34.38 ± 0.11
IFP-1 CE	5.67 ± 0.78	22.12 ± 0.85	44.99 ± 0.63	68.67 ± 2.50

[a]The D10, D50, D90, and D100 value represent the range of the particle sizes.

instantaneously start to transform into the hexagonal shaped particles after 40 min of reaction time (Figure 4).

In addition, the particle size of all IFP materials was determined via sedimentation analysis. Under MW-assisted conditions the particles of **IFP-1** possess a relatively narrow size distribution in a range from 2 to 40 μm (Table 1). The measurements showed that the statistical size distribution (Q) was not changed significantly by longer reaction times under MW-assisted conditions (Figure 5 and Table 1). For example, the mean particle size D50 (i.e., 50% particles are less than this size) of all particles is in the range of 9.12 ± 0.21 μm at t = 10 min to 13.47 ± 0.57 μm at t = 60 min. Hence, only a slight particle growth of around 4 μm is observed. The D100 value of the particle size does also show only a modest increase. This means that the particle sizes maintain their relatively uniform size as the crystallization process proceeds. In contrast, **IFP-1** synthesized under CE conditions shows a wider particle size distribution in the range from 2 to 70 μm. (Figure 5 and Table 1). The small particles of MW-assisted conditions reveal a higher nucleation rate for the crystal growth.[27,29] All other IFP materials, synthesized under CE- and MW-assisted conditions, possess a particle size distribution in a range from 2 up to 200 μm (Table S5 and S6 in the SI) and exhibit a non-specified phase with an particle size distributions with di- or polymodal character (Figures S29 and S30 in the SI). The SEM images show an inhomogeneous particle size and a mixture of nucleation phase and crystal phase (Figures S20–S26 in the SI). A disordered agglomeration of single particles was observed.

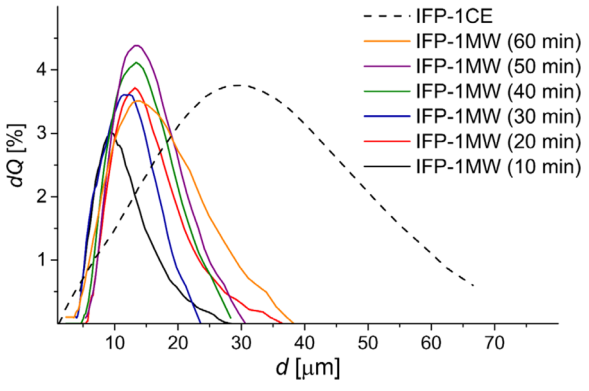

Figure 5. Particle size distribution of **IFP-1** synthesized by different reaction times under MW conditions in comparison with the IFP-1, synthesized under CE conditions.

Gas Sorption Properties. The channels of as-synthesized materials contain water and DMF molecules. The TGA traces show that after removal of the solvent, materials are stable up to 300 °C (Figure S27 in the SI). The materials are activated by degassing at 200 °C under a high vacuum (10^{-3} bar) for 24 h, prior to gas-sorption measurements. PXRD patterns of activated materials exhibit diffraction peaks similar to those of the as-synthesized sample. This indicates that the porous framework maintained the crystalline integrity after activation

DOI: 10.1021/acs.inorgchem.5b01952
Inorg. Chem. 2015, 54, 10073−10080

(Figures S8–S15 in the SI). To determine the specific surface area, we used N_2 and CO_2.

N_2 isotherms for the IFP frameworks were measured at 77.4 K up to a relative pressure p/p_0 of 0.995. The specific surface areas and micropore volume are calculated by the Brunauer–Emmett–Teller (BET) equation and the *t*-plot.[30] **IFP-1**, synthesized under MW conditions, obtained after a short reaction time of t = 10 min, exhibits a low specific surface area (a_{sBET} = 375 m^2g^{-1}) that slightly increased after t = 15 min and remains constant up to 35 min (Table 2). After 40 min of

Table 2. Comparison of the Specific Surface Areas and Micropore Volume for IFP-1 Determined by Sorption of N_2[a]

	BET method			*t*-plot	
t [min]	V_{ads} (STP)[b] [cm^3g^{-1}]	a_{sBET}[c] [m^2g^{-1}]	V_P[d] [cm^3g^{-1}]	a_1[e] [m^2g^{-1}]	a_2[f] [m^2g^{-1}]
10	113.9	375	0.173	378	7
15	152.8	512	0.255	515	8
20	163.4	536	0.247	541	10
25	166.4	544	0.254	549	9
30	157.7	524	0.238	527	10
35	176.8	574	0.270	578	9
40	229.8	763	0.351	769	8
50	233.2	777	0.357	782	18
60	225.7	769	0.345	775	9
IFP-1[g]	224.6	776	0.340	783	6

[a]Specific surface areas from N_2 sorption isotherms were calculated by the BET equation and *t*-plot. [b]Maximum N_2 adsorption capacity. [c]BET specific surface area. [d]Total pore volume. [e]Total specific surface area estimated with *t*-plot. [f]External surface area. [g]Synthesized under CE conditions.

reaction time, the enhancement of the surface area (and crystallinity) of **IFP-1** is observed (a_{sBET} = 763 m^2 g^{-1}) and remained static with time, up to 60 min. According to the PXRD patterns of **IFP-1**, it can be stated that the adsorption capacities are influenced mainly by the degree of crystallinity. The specific surface area of **IFP-1**, synthesized by MW-assisted conditions (t = 60 min, a_{sBET} = 769 m^2 g^{-1}) shows a comparable surface area to that of **IFP-1**, formed under CE conditions (t = 72 h, a_{sBET} = 776 m^2 g^{-1}).

For further comparison, we measured also the N_2 adsorption of **IFP-2** to **-5**, synthesized under CE and MW-assisted conditions (Table 3). The specific surface areas decrease from **IFP-1** to **-4** as follows: 769 m^2 g^{-1} (**IFP-1**) > 662 m^2 g^{-1} (**IFP-2**) > 499 m^2 g^{-1} (**IFP-3**) > 3 m^2 g^{-1} (**IFP-4**). This succession apparently correlates with the decreasing pore window from **IFP-1** to **-4**. Structure **IFP-4** is an apparently nonporous material with a specific surface area of only 3 m^2g^{-1}, thus nitrogen molecules apparently only populate the outer surface of the **IFP-4** crystals but cannot enter the pores. It was augmented that the ethyl chains have quite low thermal energy at 77.4 K and thus lock the pore aperture windows, keeping out nitrogen molecules like a molecular gate.[25b] The effects of different substituents of the linkers and hence tuning of the pore apertures of the zinc based IFPs obtained under MW conditions are comparable with the materials, synthesized under CE conditions (Table 3).[25a,b] However, **IFP-3**, synthesized under MW-assisted conditions, showed a slightly increased porosity (N_2 adsorption increases by ca. 25%) and specific surface area (a_{sBET} = 499 m^2 g^{-1}), in comparison with the material formed under CE methods (a_{sBET} = 324 m^2 g^{-1}).

Table 3. Comparison of the BET Specific Surface Areas and Micropore Volume for the Zn- and Co-IFPs Determined by Sorption of N_2 and CO_2[a]

Zn-IFP-n	a_{sBET}[b] [m^2g^{-1}]	V_{CO_2}[c] [cm^3 g^{-1}]	Co-IFP-n	a_{sBET}[b] [m^2g^{-1}]	V_{CO_2}[c] [cm^3 g^{-1}]
1	769 [776]	103.11 [79.37]	**5**	676 [649]	98.95 [67.83]
2	662 [622]	84.41 [81.27]	**11**	617	82.03
3	499 [324]	64.29 [46.98]	**12**	340	58.09
4	3 [0]	58.85 [56.57]	**13**	368	52.10

[a]Gas sorption data of IFPs, synthesized under CE- conditions are given in brackets. [b]Specific surface areas a_{sBET} and micropore volume V_p from N_2 sorption isotherms were calculated by the BET model. [c]Gas uptake V_{CO_2} from CO_2 isotherms were calculated from the GCMC model.[31]

The surface areas of the Co(II)-based IFPs show a comparable decrease of porosity with increasing size of the substituent, as could be expected based on the comparable structural motif. The order, **IFP-5** (676 m^2g^{-1}) > **IFP-11** (617 m^2 g^{-1}) > **IFP-12** (340 m^2 g^{-1}) (Table 3), is likely related to the Zn(II)-based imidazolate frameworks **IFP-1**, **-2**, and **-3**, respectively (Figure 6 and Table 3). The potential pore

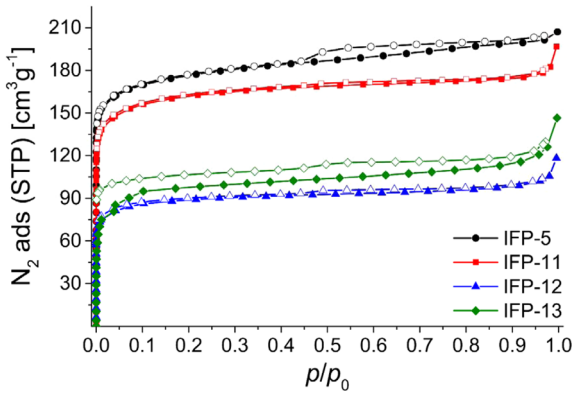

Figure 6. N_2 adsorption (closed symbols)/desorption (open symbols) isotherms of the microwave synthesized **IFP-5** (black), **IFP-11** (red), **IFP-12** (blue), and **IFP-13** (green) measured by 77 K.

windows are however reduced in size from 3.8 Å for **IFP-5**, 3.7 Å for **IFP-11**, to 3.4 Å for **IFP-12** and the hindrance for nitrogen diffusion into the pores mounted. The total pore volumes estimated from N_2 adsorption data for **IFP-5**, **-11**, and **-12** were found to be 0.32, 0.29, and 0.18 cm^3 g^{-1}, respectively. Using the *t*-plot, it can be also calculated that the outer specific surface area (a_2) is lower than 3% of the total specific surface (a_1, see the SI for details).

Interestingly, Co-based **IFP-13** exhibits a much higher specific surface of 368 m^2g^{-1} and a total pore volume of 0.22 cm^3g^{-1} than its Zn-analogue (**IFP-4**, 3 m^2g^{-1}). **IFP-13** showed a type-I isotherm, however with a broad hysteresis. In addition, N_2 adsorption of **IFP-1** to **-3** and **-5**, at 77.4 K, revealed a reversible type-I isotherm of the *H4* type hysteresis loop (Figure 6 and Figure S31 in the SI), whereas the materials, synthesized under CE conditions, showed no desorption hysteretic isotherms. The reasons can be inferred that very fast crystal growth under MW-assisted conditions may not

DOI: 10.1021/acs.inorgchem.5b01952
Inorg. Chem. 2015, 54, 10073–10080

ensure enough time for the MOF building blocks to quantitatively adhere to the growing crystal lattice at the right place, and hence, crystal defects are obtained, which lead to increased porosity.[21] We realize that the indications of broadening of the reflexes at PXRD patterns (compared to CE methods) and the characteristic type-I isotherm of the *H4* type hysteresis for N_2 adsorption could prove the crystal defects.[21b,c] Hence, to some extent mesopore formation inside microporous **IFP-3** and **IFP-13** may enhance the pore volume and specific surface areas.

The CO_2 sorption measurements at 273 and 284 K show typical type I isotherms with high gas uptake (Figure 7 and

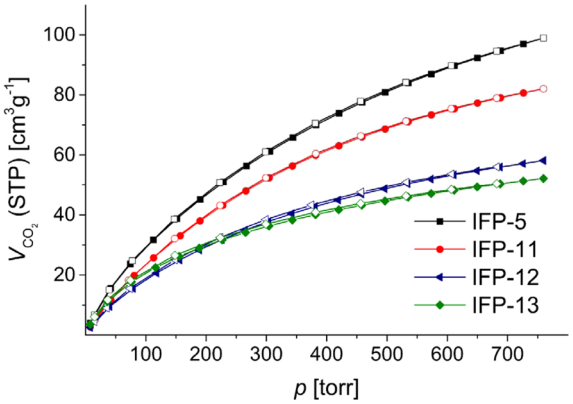

Figure 7. CO_2 adsorption (closed symbols)/desorption (open symbols) isotherms of the microwave synthesized **IFP-5** (black), **IFP-11** (red), **IFP-12** (blue), and **IFP-13** (green) measured by 273 K.

Figure S35 in the SI). The capacities of CO_2 by **IFP-11**, **-12**, and **-13** at 273 K and 1 bar are 82.03, 58.09, and 52.10 cm^3 g^{-1}, respectively, which are comparable to those of the previously reported zinc based IFPs.[25] A similar high gas uptake was found by Yaghi and co-workers for **ZIF-69** and **ZIF-82**, which were synthesized by using imidazolates containing a large choice of functional groups.[6,7] The channel diameter of **IFP-11** (3.7 Å) and **IFP-12** (3.4 Å) is slightly lower than that of **IFP-5** (3.8 Å); hence, the CO_2 uptake capacities and BET surface area are slightly lower than **IFP-5**. We believe that the IFP structures contain the 1D hexagonal channels and the gas uptake capacities depend on the size of the channel and solvent accessible void spaces.[25d] In contrast, the CO_2 uptake capacities of Co-based ZIFs (Co-**ZIF-68**, **-69**, **-81**) are higher than their isostructural Zn based analogues (Zn-**ZIF-68**, **-69**, and **-81**).[24] In such frameworks, the interaction with CO_2 presumably increases inside the Co based ZIFs compared to their Zn based analogues due to the decreased ionic radius [Zn^{2+} (0.68 Å) and Co^{2+} (0.67 Å)] and the low density of Co-ZIFs.

The enhancement of CO_2 uptake for **IFP-1** to **-5** synthesized under MW-assisted conditions could be related to the inherent defects and hence to some degree of mesopore formation during crystals growth (Table 3, Figure 8a,b, and Figure S34 in the SI).[21b,c] From the CO_2 adsorption isotherm at 273 K, the pore size distribution was derived between 4 and 10 Å by using GCMC analysis[31] and showed a relative maximum at ~3.1 Å, which is comparable with the larger channel diameter (~3.4 Å) obtained from the X-ray structure (Figure S36 in the SI). To further understand the adsorption properties, the isosteric heats of adsorption were calculated from the CO_2 adsorption isotherms at 273 and 284 K (Figure 8c), which allow the calculation of the isosteric heat of CO_2 adsorption (q_{st}=

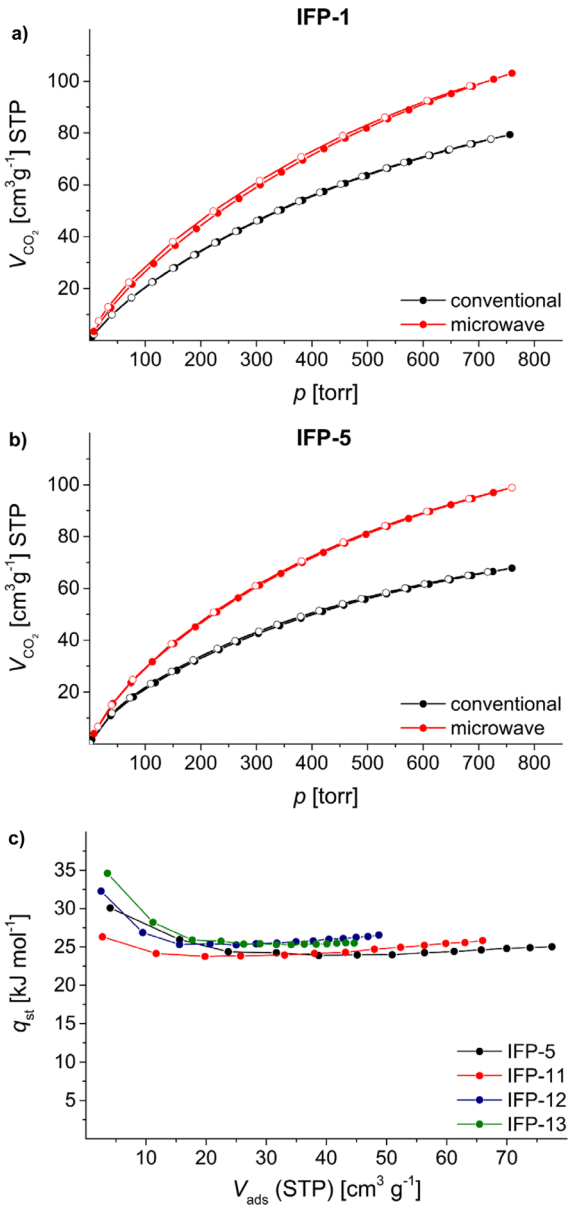

Figure 8. CO_2 adsorption (closed symbols)/desorption (open symbols) isotherms of the conventional (black) and microwave synthesized (red) (a) **IFP-1** and (b) **IFP-5** measured by T = 273 K. (c) Isosteric heat of adsorption of **IFP-5** (black), **IFP-11** (red), **IFP-12** (blue), and **IFP-13** (green).

$-\Delta H_{ads}$) as a function of loading, by using a Clausius–Clapeyron equation. At zero loading, the Q_{st} values ($-\Delta H$) are 30.1, 26.3, 32.3, and 34.6 kJ mol^{-1} for **IFP-5**, **-11**, **-12**, and **-13**, respectively, which are comparable with those for previously reported IFP materials, synthesized under solvothermal conditions.[25b] Upon increasing the loading amount, the Q_{st} value decreases to the average value to all IFP material 26 kJ mol^{-1}, which is still well above the heat of liquefaction of bulk CO_2 at 17 kJ mol^{-1}. The high Q_{st} value can be attributed to the highly polar framework and the pore size effect.

However, the materials synthesized under CE- or MW-assisted conditions could be distinguished in several analytical techniques. The PXRD patterns of the materials that are synthesized under CE method showed more sharp reflexes than the materials in MW-assisted conditions. SEM images of the CE-assisted materials were more well-shaped and crystalline

DOI: 10.1021/acs.inorgchem.5b01952
Inorg. Chem. 2015, 54, 10073–10080

wherein, MW-assisted synthesized materials are more aggregated and of nucleation form. More importantly, MW-assisted materials exhibited slight *H4* type hysteretic N_2 isotherms.

CONCLUSION

We have synthesized the isostructural 2-substituted imidazolate-4-amide-5-imidate linker based Co(II)-imidazolate frameworks (**IFP-11**, **-12**, and **-13**) under MW-assisted conditions wherein the CE synthetic way failed to produce these materials. To the best of our knowledge, for the first time, we report the *in situ* functionalization of a linker and hence MOFs formation under MW-assisted conditions in DMF. The transition from the small spherical particles (nucleation phase) into hexagonal shaped particles of IFPs was observed. The particle size measurements for all IFP materials (at CE and MW-assisted conditions) indicated that a wide size distribution existed from 2 up to 200 μm. The diameter of the channels, the polarizability, and functionality of the coordination space of IFPs can be tuned by changing the substituent at the 2-position of the linker and metal center. Moreover, it has also been demonstrated that the gas uptake capacities depend on the size of the channel and solvent accessible void spaces of the IFPs frameworks. Remarkably, the enhancement of gas uptake capacity (N_2 sorption for **IFP-3** and **-13**; CO_2 sorption for **IFP-1** to **-5**), a comparison with the materials synthesized under the CE method, could probably be the formation of a mesopore inside a micropore due to crystal defects under fast reaction MW-assisted reaction conditions.

Due to controllable pore sizes (4.2−1.7 Å) and regular channel structures of IFPs, the H_2/D_2 mixtures gas separation could be done for potential application. Moreover, the formation of defects **IFP-3**, **-5**, and **-13** under MW-assisted conditions could encourage us to study mixture gas separations (CO_2/CH_4 and N_2/CO_2) in the future.

ASSOCIATED CONTENT

Supporting Information

The Supporting Information is available free of charge on the ACS Publications website at DOI: 10.1021/acs.inorgchem.5b01952.

Experimental details, IR-spectra, PXRD patterns, SEM images, TGA analysis, gas sorption data, additional tables and figures (PDF)

AUTHOR INFORMATION

Corresponding Authors

*E-mail: suvendu.iitb@gmail.com.
*E-mail: holdt@uni-potsdam.de.

Notes

The authors declare no competing financial interest.

ACKNOWLEDGMENTS

The authors thank S. Lubahn (Universität Potsdam) for the ICP-OES measurements. We thank also Prof. Dr. A. Taubert (Institut für Chemie, Universität Potsdam) for helpful discussions concerning XRD and particle size determination. Financial support from the Deutsche Forschungsgemeinschaft is gratefully acknowledged (SPP 1362 "Porous Metal-Organic Frameworks," HO 1706/7−1 and HO 1706/7−2).

REFERENCES

(1) (a) Jacobson, M. Z. *Energy Environ. Sci.* **2009**, *2*, 148−173. (b) D'Alessandro, D. M.; Smit, B.; Long, J. R. *Angew. Chem., Int. Ed.* **2010**, *49*, 6058−6082.

(2) Keskin, S.; van Heest, T. M.; Sholl, D. S. *ChemSusChem* **2010**, *3*, 879−891.

(3) (a) MacGillivray, L. R. *Metal-Organic Frameworks: Design and Application*; John Wiley & Sons: Hoboken, NJ, 2010. (b) Farrusseng, D. *Metal-Organic Frameworks Applications from Catalysis to Gas Storage*; Wiley-VCH: Weinheim, Germany, 2011.

(4) Sumida, K.; Rogow, D. L.; Mason, J. A.; McDonald, T. M.; Bloch, E. D.; Herm, Z. R.; Bae, T.-H.; Long, J. R. *Chem. Rev.* **2012**, *112*, 724−781.

(5) Li, J.-R.; Sculley, J.; Zhou, H.-C. *Chem. Rev.* **2012**, *112*, 869−932.

(6) Phan, A.; Doonan, C. J.; Uribe-Romo, F. J.; Knobler, C. B.; O'Keeffe, M.; Yaghi, O. M. *Acc. Chem. Res.* **2010**, *43*, 58−67.

(7) Banerjee, R.; Furukawa, H.; Britt, D.; Knobler, C.; O'Keeffe, M.; Yaghi, O. M. *J. Am. Chem. Soc.* **2009**, *131*, 3875−3877.

(8) (a) Klimakow, M.; Klobes, P.; Thunemann, A. F.; Rademann, K.; Emmerling, F. *Chem. Mater.* **2010**, *22*, 5216−5221. (b) Friščić, T. *Chem. Soc. Rev.* **2012**, *41*, 3493−3510. (c) Prochowicz, D.; Sokołowski, K.; Justyniak, I.; Kornowicz, A.; Fairen-Jiminez, D.; Friščić, T.; Lewiński, J. *Chem. Commun.* **2015**, *51*, 4032−4035.

(9) (a) Ameloot, R.; Stappers, L.; Fransaer, J.; Alaerts, L.; Sels, B. F.; de Vos, D. E. *Chem. Mater.* **2009**, *21*, 2580−2582. (b) Stassen, I.; Styles, M.; van Assche, T.; Campagnol, N.; Fransaer, J.; Denayer, J.; Tan, J.-C.; Falcaro, P.; de Vos, D.; Ameloot, R. *Chem. Mater.* **2015**, *27*, 1801−1807.

(10) Garcia Marquez, A.; Horcajada, P.; Grosso, D.; Férey, G.; Serre, C.; Sanchez, C.; Boissiere, C. *Chem. Commun.* **2013**, *49*, 3848−3850.

(11) (a) Li, Z.-Q.; Qiu, L. G.; Xu, T.; Wu, Y.; Wang, W.; Wu, Z. Y.; Jiang, X. *Mater. Lett.* **2009**, *63*, 78−80. (b) Yang, D.-A.; Cho, H.-Y.; Kim, J.; Yang, S.-T.; Ahn, W.-S. *Energy Environ. Sci.* **2012**, *5*, 6465−6473. (c) Thompson, J. A.; Chapman, K. W.; Koros, W. J.; Jones, C. W.; Nair, S. *Microporous Mesoporous Mater.* **2012**, *158*, 292−299.

(12) (a) Klinowski, J.; Paz, F. A. A.; Silva, P.; Rocha, J. *Dalton Trans.* **2011**, *40*, 321−330. (b) Flügel, E. A.; Ranft, A.; Haase, F.; Lotsch, B. V. *J. Mater. Chem.* **2012**, *22*, 10119−10133. (c) Wu, X.; Bao, Z.; Yuan, B.; Wang, J.; Sun, Y.; Luo, H.; Deng, S. *Microporous Mesoporous Mater.* **2013**, *180*, 114−122. (d) Liang, W.; D'Alessandro, D. M. *Chem. Commun.* **2013**, *49*, 3706−3708. (e) Khan, N. A.; Jhung, S. H. *Coord. Chem. Rev.* **2015**, *285*, 11−23.

(13) McDonald, T. M.; D'Alessandro, D. M.; Krishna, R.; Long, J. R. *Chem. Sci.* **2011**, *2*, 2022−2028.

(14) Rabone, J.; Yue, Y. F.; Chong, S. Y.; Stylianou, K. C.; Bacsa, J.; Bradshaw, D.; Darling, G. R.; Berry, N. G.; Khimyak, Y. Z.; Ganin, A. Y.; Wiper, P.; Claridge, J. B.; Rosseinsky, M. J. *Science* **2010**, *329*, 1053−1057.

(15) Choi, H. S.; Suh, M. P. *Angew. Chem., Int. Ed.* **2009**, *48*, 6865−6869.

(16) Hong, D. H.; Suh, M. P. *Chem. Commun.* **2012**, *48*, 9168−9170.

(17) Henke, S.; Fischer, R. A. *J. Am. Chem. Soc.* **2011**, *133*, 2064−2067.

(18) Caskey, S. R.; Wong-Foy, A. G.; Matzger, A. J. *J. Am. Chem. Soc.* **2008**, *130*, 10870−10871.

(19) Seo, J.; Matsuda, R.; Sakamoto, H.; Bonneau, C.; Kitagawa, S. *J. Am. Chem. Soc.* **2009**, *131*, 12792−12800.

(20) An, J.; Geib, S. J.; Rosi, N. L. *J. Am. Chem. Soc.* **2010**, *132*, 38−39.

(21) (a) Fang, Z.; Bueken, B.; de Vos, D. E.; Fischer, R. A. *Angew. Chem., Int. Ed.* **2015**, *54*, 7234−7254. (b) Park, J.; Wang, Z. Y. U.; Sun, L. B.; Chen, Y. P.; Zhou, H. C. *J. Am. Chem. Soc.* **2012**, *134*, 20110−20116. (c) López-Maya, E.; Montoro, C.; Colombo, V.; Barea, E.; Navarro, J. A. R. *Adv. Funct. Mater.* **2014**, *24*, 6130−6135. (d) Trickett, C. A.; Gagnon, K. J.; Lee, S.; Gándara, F.; Bürgi, H.-B.; Yaghi, O. M. *Angew. Chem., Int. Ed.* **2015**, *54*, 11162−11167. (d1) Ravon, U.; Savonnet, M.; Aguado, S.; Domine, M. E.; Janneau, E.; Farrusseng, D. *Microporous Mesoporous Mater.* **2010**, *129*, 319−329. (e) Furukawa,

DOI: 10.1021/acs.inorgchem.5b01952
Inorg. Chem. 2015, 54, 10073−10080

H.; Muller, U.; Yaghi, O. M. *Angew. Chem., Int. Ed.* **2015**, *54*, 3417−3430.
(22) (a) Luebke, R.; Eubank, J. F.; Cairns, A. J.; Belmabkhout, Y.; Wojtasb, L.; Eddaoudi, M. *Chem. Commun.* **2012**, *48*, 1455−1457. (b) Vaidhyanathan, R.; Iremonger, S. S.; Shimizu, G. K. H.; Boyd, P. G.; Alavi, S.; Woo, T. K. *Science* **2010**, *330*, 650−653. (c) Chen, B.; Ockwig, N. W.; Millward, A. R.; Contreras, D. S.; Yaghi, O. M. *Angew. Chem., Int. Ed.* **2005**, *44*, 4745−4749. (d) An, J.; Rosi, N. L. *J. Am. Chem. Soc.* **2010**, *132*, 5578−5579. (e) Bourrelly, S.; Llewellyn, P. L.; Serre, C.; Millange, F.; Loiseau, T.; Ferey, G. *J. Am. Chem. Soc.* **2005**, *127*, 13519−13521.
(23) (a) Yu, D.; Yazaydin, A. O.; Lane, J. R.; Dietzel, P. D. C.; Snurr, R. Q. *Chem. Sci.* **2013**, *4*, 3544−3556. (b) Dietzel, P. D. C.; Besikiotis, V.; Blom, R. *J. Mater. Chem.* **2009**, *19*, 7362−7370. (c) Valenzano, L.; Civalleri, B.; Chavan, S.; Palomino, G. T.; Arean, C.; Bordiga, S. *J. Phys. Chem. C* **2010**, *114*, 11185−11191. (d) Mason, J. A.; Sumida, K.; Herm, Z. R.; Krishna, R.; Long, J. R. *Energy Environ. Sci.* **2011**, *4*, 3030−3040. (e) Kong, X.; Scott, E.; Ding, W.; Mason, J. A.; Long, J. R.; Reimer, J. A. *J. Am. Chem. Soc.* **2012**, *134*, 14341−14344.
(24) Panda, T.; Gupta, K. M.; Jiang, J.; Banerjee, R. *CrystEngComm* **2014**, *16*, 4677−4680.
(25) (a) Debatin, F.; Thomas, A.; Kelling, A.; Hedin, N.; Bacsik, Z.; Senkovska, I.; Kaskel, S.; Junginger, M.; Müller, H.; Schilde, U.; Jäger, C.; Friedrich, A.; Holdt, H.-J. *Angew. Chem., Int. Ed.* **2010**, *49*, 1258−1262. (b) Debatin, F.; Behrens, K.; Weber, J.; Baburin, I. A.; Thomas, A.; Schmidt, J.; Senkovska, I.; Kaskel, S.; Kelling, A.; Hedin, N.; Bacsik, Z.; Leoni, S.; Seifert, G.; Jäger, C.; Günter, C.; Schilde, U.; Friedrich, A.; Holdt, H.-J. *Chem. - Eur. J.* **2012**, *18*, 11630−11640. (c) Mondal, S. S.; Bhunia, A.; Demeshko, S.; Kelling, A.; Schilde, U.; Janiak, C.; Holdt, H.-J. *CrystEngComm* **2014**, *16*, 39−42. (d) Mondal, S. S.; Thomas, A.; Holdt, H.-J. *Microporous Mesoporous Mater.* **2015**, *216*, 2−12.
(26) (a) Yanagisawa, H.; Amemiya, Y.; Kanazaki, T.; Shimoji, Y.; Fujimoto, K.; Kitahara, Y.; Sada, T.; Mizuno, M.; Ikeda, M.; Miyamoto, S.; Koike, H. *J. Med. Chem.* **1996**, *39*, 323−338. (b) Coad, E. C.; Kampf, J.; Rasmussen, P. G. *J. Org. Chem.* **1996**, *61*, 6666−6672. (c) Rasmussen, P. G.; Apen, P. G. *Heterocycles* **1989**, *29*, 1325−1329.
(27) (a) Haque, E.; Jhung, S. H. *Chem. Eng. J.* **2011**, *173*, 866−872. (b) Tompsett, G.; Conner, W. C.; Yngvesson, K. S. *ChemPhysChem* **2006**, *7*, 296−319. (c) Park, S.-E.; Chang, J.-S.; Hwang, Y. K.; Kim, D. S.; Jhung, S. H.; Hwang, J.-S. *Catal. Surv. Asia* **2004**, *8*, 91−110.
(28) Spek, A. L. *PLATON*; Utrecht University: Utrecht, The Netherlands, 2001.
(29) Jhung, S. H.; Jin, T.; Hwang, Y. K.; Chang, J.-S. *Chem. - Eur. J.* **2007**, *13*, 4410−4417.
(30) Lippens, B. C.; de Boer, J. H. *J. Catal.* **1965**, *4*, 319−323.
(31) (a) Vishnyakov, A.; Ravikovitch, P. I.; Neimark, A. V. *Langmuir* **1999**, *15*, 8736−8742. (b) Rodriguez-Reinoso, F.; Linares-Solano, A. *Chemistry and Physics of Carbon*; Thrower, P. A., Ed.; Marcel Dekker: New York, 1988; Vol. *21*.

DOI: 10.1021/acs.inorgchem.5b01952
Inorg. Chem. 2015, 54, 10073−10080